ACS OMEGA

Open Access

http://pubs.acs.org/journal/acsodf

Article

Gear-Shaped High-*g* Combustion Chamber for Micro Turbojet Engine Applications

Haozhong Huang,* Guixin Chen, Huigui long, Baijun Lei, and Jianguo Liang

Cite This: *ACS Omega* 2024, 9, 18674−18685

Read Online

ACCESS | Metrics & More | Article Recommendations

ABSTRACT: Enhancing combustion efficiency and optimizing the thrust-to-weight ratio are critical technical challenges encountered in the development, application, and growth of micro turbojet engines. The high-centrifugal (high-*g*) combustion chamber, as an innovative combustion chamber system, has the capability to replace the primary combustion chamber of the traditional turbojet engine, reducing the length of the combustion chamber while maintaining engine performance. Previous studies on the structure of the high-*g* combustor (HGC) have shown problems such as uneven temperature distribution of the turbojet rotor. To improve the feasibility of HGC integration into micro turbojet engines, this study conducts relevant experiments on a 120 N thrust engine. Subsequently, the results of these experiments were used to analyze the structural design of HGC through a simulation approach. Including six main configurations, the first four structural designs focused on establishing a suitable highly centrifugal environment to stabilize and improve the combustion performance, which was successfully achieved by designing the outer ring gear-shaped inlet with four different angles. Subsequent structural designs were based around improving the uniformity of the temperature distribution at the combustion chamber outlet. The final design of the HGC combustion efficiency is not much different from the original combustion chamber, and it can shorten the axial length of the combustion chamber by nearly 30%. The design of the air inlet holes and the baffle plate effectively improves the temperature uniformity at the outlet of the combustion chamber. Moreover, without changing the combustion chamber material, the corresponding engine weight can be reduced by about 10.7%, and the engine thrust-to-weight ratio can be improved by up to 12% with the same thrust, which provides design ideas for further lightweight applications.

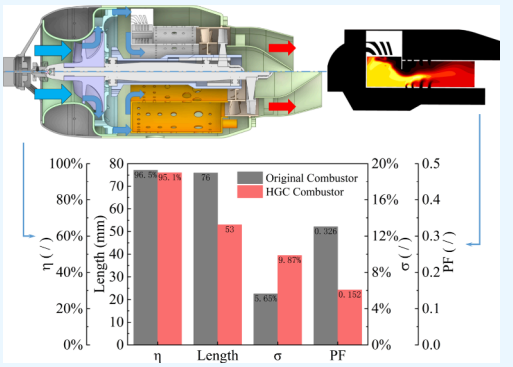

1. INTRODUCTION

Micro turbine engines have a wide range of applications in propulsion systems and energy owing to their small size, low cost, high energy density, and high thrust-to-weight ratio. High-performance turbojet engines play an important role in military applications. In recent decades, to improve the efficiency of turbojet engines as well as the thrust-to-weight ratio, Sirignano and Liu[1] proposed the concept of an inter-turbine burner (ITB), in which a new combustion chamber is introduced between the high- and low-pressure turbine stages or in the passages between the turbine blades; this can help increase the thrust and maintain a low fuel consumption rate. However, the shorter length of the combustion chamber between the blades makes it more difficult to achieve stable combustion. The Air Force Research Laboratory (AFRL) designed and developed an ultra-compact combustion (UCC) series of combustion chambers based on the research of Lewis[2] and combined them with a standing vortex. By using centrifugal loading, a high-vortex environment is established in the combustion chamber, which induces a full mixing of the fuel and the air to increase the flame propagation rate. In addition, compared with conventional combustion chambers, the UCC series of combustion chambers can shorten the axial length by more than 50% while guaranteeing combustion performance.[3] UCC chambers were intended to solve the application of ITBs in tight spaces; however, their excellent combustion performance has led to their gradual adoption as an alternative to the main combustion chambers or combustion chamber geometries for turbine engines. UCC chambers are currently categorized into two main types: The first is known as the trapped-vortex combustor (TVC), which was first evaluated by Hsu et al.[4] and has been studied for decades owing to its simple geometry and good performance;[5,6] the second is known as the high-*g* combustor (HGC). Figure 1 shows a schematic comparison of the two types of combustion chambers, both of which are designed with an

Received: March 1, 2024
Revised: March 29, 2024
Accepted: April 3, 2024
Published: April 12, 2024

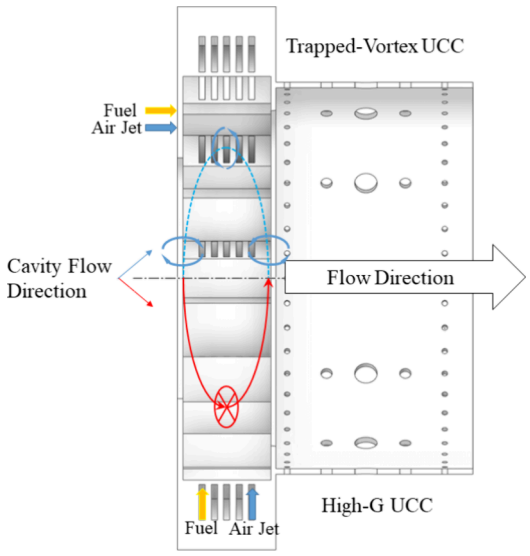

Figure 1. Schematic comparison of HGC and TVC.

annular cavity, which is used to generate and stabilize the vortex, the difference being that the axis of the vortex in the TVC is tangent to the circumference of the cavity, whereas the axis of the vortex in the HGC is aligned with the axis of the cavity.[7]

The most notable difference is that the central axis of the vortex generated by the TVC is tangential to the circumference of the chamber whereas in the case of the HGC, the axis of the vortex remains in line with the axis of the combustion chamber.

The first application of the high-g technique to UCC was performed by Lewis,[2] who used a combustion centrifuge to study premixed combustion at a high centrifugal acceleration. The experimental results showed that the flame velocity of propane/air mixtures in a high-g acceleration field was nearly four times that of a conventional turbulent flame. Lewis explained this phenomenon by proposing a hypothesis based on the "bubble transport" flame diffusion mechanism, defining g-loading using the dimensionless number g, which has been used ever since, where g is the centrifugal acceleration, g_0 is the gravitational acceleration, u_{tan} is the tangential velocity, and r is the radial distance from the center of rotation.

$$g - \text{loading} = \frac{g}{g_0} = \frac{u_{tan}^2}{rg_0} \tag{1}$$

Subsequently, Yonezawa et al.[8] proposed the "vortex burst mechanism", the essence of which is that combustion gases are directed to the rotation axis by the pressure gradient generated by the centrifugal action of the cyclone, thus accelerating the flame propagation speed. They also suggested that the combustion efficiency may be influenced via eq 2:

$$\eta \propto \frac{\tau_r}{\tau_m + \tau_c} \tag{2}$$

Using this equation, Yonezawa et al. improved the combustion efficiency by decreasing the combustion time (τ_c) and the mixing time between fuel and air (τ_m) or increasing the residence time (τ_r). They proved computationally and experimentally that jet cyclone combustion chambers can generate directional vortices to increase the residence time and reaction rate to achieve the same combustion efficiency as that of conventional combustion chambers or even higher. Zelina et al.[9,10] started developing an early HGC structure. The initial HGC structure is simple but highly representative. It mainly consists of an annular cavity, a center body, a set of guide vanes, an air jet inlet, and a fuel nozzle. The air jet inlet is responsible for generating a strong vortex and mixing with the fuel in the annular cavity to form a rich combustion environment, which is the main area of high-g combustion. The mainstream cold air is diverted to the lower part of the annular cavity by the guide vanes such that part of the flame in its vicinity is quickly extinguished and the rest of the flame undergoes lean combustion in the guide vane passages, which is used to suppress NOx production. Overall, the purpose of the structure is to create a rich flame in the annular cavity and high-g combustion, quenching in the vicinity of the guide vanes, and lean combustion in the guide vane passages, which is known as the rich-burn, quick-quench, lean-burn (RQL) combustion process.[11]

In addition, Zelina et al.[9,10] experimentally loaded with a load of approximately 3000 g_0 to increase the reaction rate, which can realize complete combustion in a compact space with an axial distance of approximately 30−50% of that of a conventional combustion chamber. Under the same conditions, the flame-burning length under HGC operation was only approximately 50% that of the conventional combustion chamber and a combustion efficiency of more than 98% could be obtained under high-pressure conditions.

The superior combustion performance of high-g technology has motivated many researchers to conduct experiments to verify this phenomenon,[12−14] and numerous studies have been conducted to obtain a more detailed flame mechanism through simulations.[15−18] Recently, researchers have pointed out that the high-g combustion mechanism is more complex and may be related to the Rayleigh−Taylor instability.[16−18] Briones et al.[17] reproduced Lewis's experiments using a two-dimensional computational domain to simulate a rotating combustion tube and found that higher values of g-loading were not better, and at larger values of g-loading, the flame front broke up and disrupted its own mixing with the fuel, which led to localized quenching and slowed down flame propagation. Briones proposed that Rayleigh−Taylor instability affects the localized flow rate of the flame and thus the flame propagation rate.

Research projects and design iterations on HGCs are still ongoing, and although the geometries are different from those of the HGC prototypes, the principles are similar. Greenwood et al.[19] designed an HGC with an additional cavity and found that as the centrifugal acceleration of the gas was increased, the pressure drop in the combustion chamber increased. Despite this, it will be more friendly to pollutant emissions. Anisko et al.[20] optimized the design of an HGC cavity by designing the blade shape such that the vortex is forced to remain in the annular cavity to further reduce the HGC volume and maximize the use of the annular cavity. Conrad et al.[21] designed an HGC with a variable diffuser to separate the pressurizer outlet flow into annular cavity and core flows, which was used to solve the problem of connecting the annular flow to the axial flow. Bohan and Polanka and Blunck et al.[22,23] further reduced the length and weight of the engine by eliminating the pressurizer outlet guide vanes and combining the UCC with neighboring components. The single-chamber combustion chamber could withstand a higher g-loading under the same conditions, and a more uniform temperature distribution could be obtained using a flame stabilizer. Wilson

https://doi.org/10.1021/acsomega.4c02030
ACS Omega 2024, 9, 18674−18685

et al.[14] further improved the mixing guide vane based on their predecessors; however, a secondary air injection was still required to produce a high-*g* environment in the cavity. The HGC design of Erdmann et al.[24] adopts the form of a secondary cavity so that the fuel can be completely atomized and sprayed into the vortex. The results showed that the combustion efficiency was not significantly affected by different jet-air angles, the combustion efficiency was still approximately 99%, and the NOx emission decreased with an increase in *g*-loading. Cottle et al.[25] added a set of injection plates and baffles to an HGC with a diffuser to control the directions and ratios of the core and secondary streams.

Subsequently, Bohan et al.[26,27] designed a cooling scheme by designing holes to form a cooling film and hence mitigate the localized overheating problem of the HGC. Zhang et al.[6] designed an asymmetric combustion chamber, and the experimental results showed that the combustion efficiency was greater than 94%. The combustion efficiency, dynamic pressure characteristics, and emissions were found to be affected by the inlet injection velocity, and the main combustion chamber volume and flame structure of the stabilizer had different degrees of influence on the combustion and stabilization characteristics. In addition, Bohan and Polanka and Liu et al.[28−30] investigated methods for adapting the HGC to a micro turbojet engine and found that the new HGC design could reduce the axial length of the engine.

Most existing HGCs focus on large and medium-sized turbine engines, and there is a lack of research on micro turbojet engines, which have broad application prospects with the popularization of unmanned aerial vehicles. The feasibility of HGC in a micro turbojet engine is evaluated to improve the efficiency and thrust-to-weight ratio of a micro turbojet engine. Experiments related to ground testing of an engine with a thrust of 120 N were conducted to collect the necessary data to carry out structural design and simulation calculations for the HGC. The effects of different schemes on combustion performance were analyzed to provide guidance for the development and design of miniature turbojet engines.

2. METHODOLOGY

2.1. Experimental Method. Before the structure of the HGC was designed, a test rig with a safety enclosure was designed to collect test data on a 120 N thrust engine with an overall length of 250 mm, outer diameter of 99.4 mm, net weight of 1250 g, and maximum sustainable thrust of 120 N. Figure 2 illustrates the cross section of the engine. The main structure had a centrifugal compressor and an axial turbine, and the outlet of the compressor had deflector vanes to ensure that the airflow flowed in the axial direction to the combustion chamber.

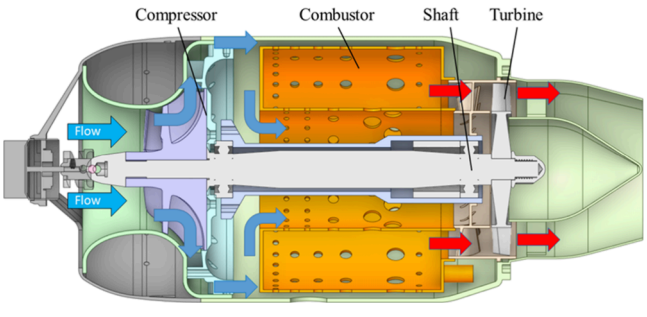

Figure 2. Engine cross-sectional fluid flow path.

The test rig is mainly used to obtain necessary data such as the temperature, pressure, thrust, and mass flow of the engine for further analysis and research design. Figure 3 illustrates several parts of the test rig, including the intake duct, engine, exhaust duct, and data acquisition system. It incorporates thermal gas mass flow meters and elliptical gear flow meters, both with an accuracy of ±0.5% of full scale. The engine was mounted on a sliding bracket that was connected to the slide rails by a set of ball bearing sliders. The sliding bracket was connected to one end of the force transducer, and the other end of the transducer was connected to the anchor of the test rig, which outputs the thrust through the force transducer. The accuracy of the force transducer was determined via a ±0.03% nonlinearity of the full-scale value of 20 kg and a ±0.03% hysteresis of the full-scale value. In situ calibration was performed, and the signal was amplified by a charge amplifier and then transmitted to the signal acquisition box. In addition, several temperature and pressure sensors were installed on the engine, the locations of which are shown in Figure 3. All the temperature measurements were performed using type-K thermocouples, and the accuracy of the temperature and pressure sensors was ±0.5% of the full scale.

During the experiment, ECUctrl_ZK software was used to control the throttle position of the engine. All data were collected before engine ignition until the engine reached a maximum thrust. Moreover, the oil pump was maintained for at least 30 s during each run, so that data could be collected multiple times at specific engine speeds. Finally, the collected data were processed for uncertainty analysis.[31] Table 1 lists the measured data for the cruise condition at approximately 80% power, which were used as the boundary conditions in later simulations with a maximum relative error of less than 4%.

2.2. Simulation Model. A new HGC structure was researched and designed to develop an alternative combustion chamber for micro turbojet engines. The developed HGC had a minimum inner diameter of 22.5 mm and a maximum outer diameter of 96 mm. The minimum inner diameter was designed to be adaptable to the turbine stator of the original engine. By analyzing and summarizing previous studies,[2,9,10,25] early HGCs were found to mainly consist of a main inlet, auxiliary inlet holes, and mixing guide vanes, making them relatively complex structures that cannot be easily integrated into micro turbojet engines. The new HGC structure is specific to the miniature turbojet engine, which creates a main combustion region based on the original annular flame cylinder combustion chamber so that the fuel is burned in a high-*g* environment. To satisfy the conditions for high-*g* formation, the focus of the new structure is the design of the air inlet, which directs the air from the axial to circumferential direction, creating a cyclonic flow in the main combustion region and a suitable high-*g* environment to ensure fast and stable combustion. The flow distributions in the main combustion region and other regions must also be considered to ensure complete combustion and a more uniform outlet temperature. Figure 4 illustrates the four air inlet designs with the combustion chamber inlet plane positioned horizontally, tilted at 30 and 60°, and vertically at 90°. It should be mentioned that the idea is not unique, since a similar design was researched by Bohan and Polanka.[28]

Twelve air inlets were created throughout the combustion chamber to direct the airflow to the desired jet angle and create

https://doi.org/10.1021/acsomega.4c02030
ACS Omega 2024, 9, 18674−18685

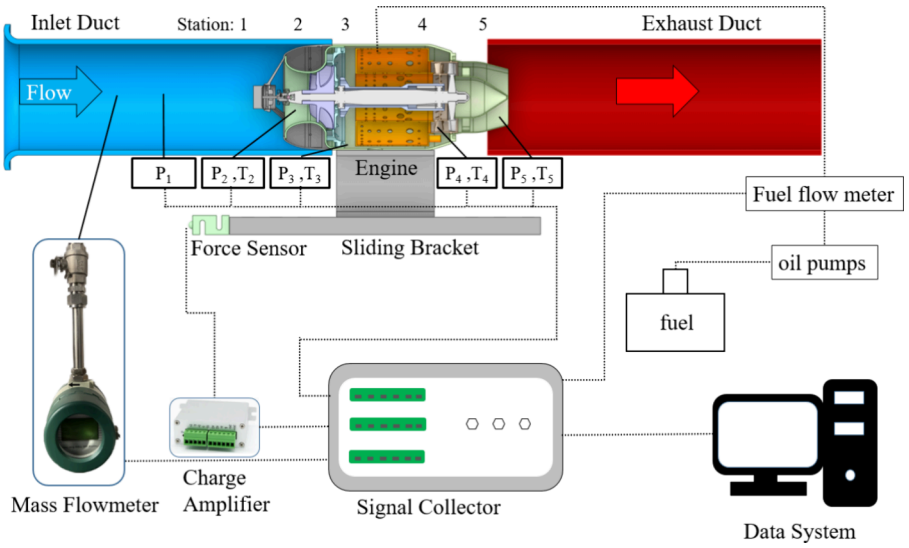

Figure 3. Schematic diagram of the test system.

Table 1. Experimental Data and Relative Error Analysis under 80% Engine Power Cruising Condition

	T_3	T_4	P_3	m_{in}	thrust
value	316 K	906 K	0.24 MPa	0.24 kg/s	95 N
relative error	0.62%	0.44%	2.08%	3.33%	1.05%

a large and uniform vortex. However, the pressure distribution changed largely with different designs and the calculated total area would be readjusted after several computational fluid dynamics simulations were performed in each design case. Figure 5 demonstrates the fitting of the HGC to the 120 N thrust engine for easy comparison, revealing that the geometry of the HGC was considerably shorter than that of the original combustion chamber, with a significantly farther distance from the pressurized outlet to the front wall surface of the combustion chamber. Furthermore, a reduction in the axial length of more than 30% was achieved.

2.3. Calculation Domain and Mesh Settings. All of the studied scenarios were analyzed by simulating the computational region from the pressurizer outlet to the combustion chamber outlet. The pressurizer outlet served as the air inlet to the computational domain, the air entered the combustion chamber, and the fuel entered the combustion chamber through the injection ports to be atomized. The combustion chamber was geometrically simplified by omitting components, such as the igniter and fuel line. The fuel was injected as a liquid spray through fuel injectors, and a discrete phase was used to model the transition of the liquid fuel spray into the gas phase. This is achieved by employing both Eulerian and Lagrangian frames of reference. Figure 6 illustrates the computational domain for configuration 4 (C4). Owing to the rotational periodicity of the computational area around the

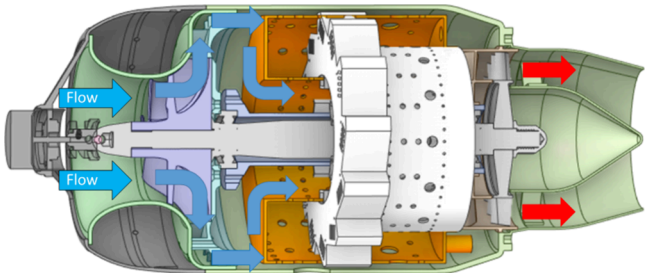

Figure 5. Schematic of the engine cross section with HGC configuration 1 compared with the original combustion chamber.

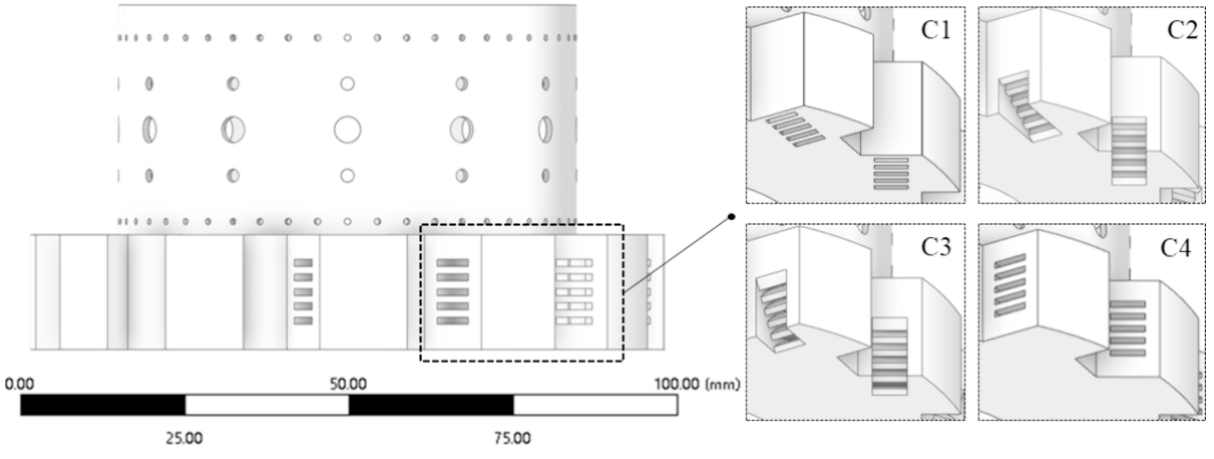

Figure 4. Four inlet configurations of the HGC.

https://doi.org/10.1021/acsomega.4c02030
ACS Omega 2024, 9, 18674−18685

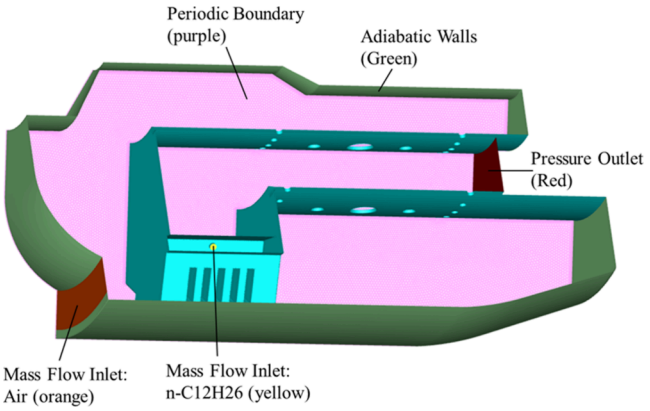

Figure 6. Computing domains for C4.

central axis of the engine, the computational domain could be simplified by setting up periodic boundaries. In this study, a 30° sector-shaped region was used for analysis.

After determining the computational region, an initial estimation of the mesh characteristics was performed according to the designed HGC scheme while the maximum laminar flame thickness was in the range 0.6−1.4 mm, which was derived from the following equation.[30]

$$\delta_L = 2(\lambda/\rho C_P S_L)(T_2/T_1)^{0.7} \quad (3)$$

where δ_L is the estimated laminar flame thickness, λ is the thermal conductivity, C_P is the specific heat capacity, and S_L is the laminar flame speed, and T_1, and T_2 are the temperatures of the unburned and post-burned mixtures, respectively. Based on the estimation results, the initial wall mesh size and growth rate must be determined to ensure that the boundary layer mesh is created at the wall with sufficient mesh resolution; at least 10 layers of boundary mesh are required. The height of the first boundary layer was also set to 0.002 mm so that the $y+$ value was less than 5 for most of the conditions; this ensured correct heat transfer calculations. The computational region was hybrid meshed using fluent meshing, first into a tetrahedral surface mesh and subsequently into a hexahedral mesh for fluid, and when a hexahedral mesh could not be generated owing to geometry or interference from neighboring cells, the mesh generator used polyhedral cells to fill the remaining volume.

2.4. Computational Settings. The current structural design iterations for combustion chambers rely heavily on simulation methods. Simulation studies were performed using the commercial software FLUENT with a pressure-based run solver. Due to the complex composition of PR-3, this study used the JetSurf 1.0 chemical reaction mechanism,[32] which contains 194 component and 1459 primitive reactions, which were added as an input to the model to more accurately calculate combustion values in FLUENT. The discrete-phase model was used to simulate *n*-dodecane spray in a preheat tube.

The remainder of the computational setup was based on previous works by Bohan,[28] Liu,[30] Cottle,[33] and others, who all performed experimental investigations for comparison with simulation results; these were used to validate the CFD computational setup for the turbulent combustion of the HGC. The realizable $k-\varepsilon$ model was selected for the turbulence model. A partially premixed combustion FGM model was used as the combustion model. The small-flame model assumes that the reaction zone of the turbulent flame is thinner than the smallest scale of turbulent pulsation and that the turbulent diffusion flame is considered to be a moving diffusive laminar flame surface. The inlet fluid to the computational domain was defined as air (containing only 79% nitrogen and 21% oxygen), and the fuel and air distributions in the computational domain were controlled by the mixing probability distribution function (PDF) computed by using FLUENT. Table 2 lists the inlet and outlet boundary conditions for the 30° sector computational domain, and the values in the table correspond to an inlet mass flow rate of 0.232 kg/s for a 120 N thrust engine. These data were obtained from the experimental data collected under the specified conditions for the engine under cruise conditions near 80% power when the engine operated at a pressure of 245 kPa, which was the experimental data obtained under the specified conditions. This pressure was defined as the operating pressure in the simulation. The fuel and air flow rates mentioned above result in a engine global equivalence ratio of 0.33. The outlet temperatures in Table 2 used calculated engine exhaust gas temperatures and average temperature values at the outlet plane.

Table 2. Import and Export Boundary Conditions in the Computational Domain

item	air Inlet	fuel inlet	outlet
mass flow rate (kg/s)	0.0193	0.000389	N/A
gauge pressure (Pa)	3800	50,000	0
temperature (K)	320	300	960

The "coupled" pressure−velocity coupling scheme was chosen to solve for pressure and velocity as a linked pair, with the least squares cell-based method for the gradient and second-order interpolation for the pressure discretization. Spatial discretization was selected as second-order upwind to reduce numerical spread and inaccuracies and to make the results reliable. The solution was solved in the steady state, the pseudotransient was turned on to accelerate the convergence, and the residuals of the key quantities are established to ensure that the steady-state solution was realized in the case of very small oscillations.

2.5. Evaluation Parameters. The most important evaluation parameters of this study are shown in the following equation:[34]

$$\eta = 1 - 10109\frac{EI_{CO}}{H_C} - \frac{EI_{C_xH_y}}{1000} \quad (4)$$

where η denotes the combustion efficiency, which is one of the main evaluation parameters, EI_{CO} represents the emission index of carbon monoxide, $EI_{C_xH_y}$ denotes the emission index of unburned hydrocarbons, and H_C denotes the net heat of fuel combustion. The total pressure loss coefficient σ is defined as

$$\sigma = 1 - \frac{P_{t4}}{P_{t3}} \quad (5)$$

where P_{t4} represents the combustion chamber outlet total pressure and P_{t3} represents the combustion chamber inlet total pressure. Another important evaluation parameter for the combustion chamber is the pattern factor (PF); PF is used to measure the temperature uniformity at the exit plane of the combustion chamber and describes the deviation of the maximum exit temperature (T_{4max}) from the average exit

https://doi.org/10.1021/acsomega.4c02030
ACS Omega 2024, 9, 18674−18685

temperature (T_{4avg}) by comparing it with the difference between the average combustion chamber exit temperature and the inlet temperature (T_3), which is defined as follows.[35]

$$\mathrm{PF} = \frac{T_{4max} - T_{4avg}}{T_{4avg} - T_3} \tag{6}$$

2.6. Model Validation. The mesh convergence analysis was performed on the combustion chamber of the 120 N thrust engine, and the number of meshes of the primitive combustion chamber was divided into approximately 6, 8, and 10 million meshes, after which the representative mesh size, h, defined below could be estimated based on the primitive combustion chamber mesh convergence method.[36]

$$h = \left[\frac{1}{N}\sum_{i=1}^{N}(\Delta V_i)\right]^{1/3} \tag{7}$$

where ΔV_i is the volume of the ith grid cell and N is the total number of grid cells in the computational domain. The relative parameters for the grid independence analysis are given in Table 3. The combustion chambers with all three grid quantities were computed using the same boundary conditions and computational settings. The geometry of the original combustion chamber was checked for grid independence, which was simpler in shape and larger in volume relative to the geometry of the UCC chamber, and according to the derivation of eq 7, the representative grid of the UCC chamber will be smaller for the same grid resolution. When fluid motion and fuel combustion can be obtained in the grid of the original combustion chamber with more accurate simulations, the combustion chamber in other configurations can also be computationally analyzed at the same grid resolution.

Table 3. Lattice Convergence Analysis

item	1	2	3
number of nodes (/)	6,252,560	8,044,913	9,883,106
h (mm)	0.204	0.188	0.176
total pressure loss (/)	5.60%	5.65%	5.69%

In addition, on the left side of Figure 7, the plot shows the average temperature in the normalized region of the combustion chamber as a function of the normalized axial position for the three grid sizes. The normalized value of the temperature was taken as the ratio of the difference between the local and inlet temperatures to the difference between the maximum and the inlet temperatures.

The resolutions of the three grids are shown in Table 3 and were approximately 6.25 million, 8.04 million, and 9.88 million grid counts. From 6.25 million to 8.04 million grids, the number of grids increased by approximately 28.67% and the maximum temperature difference ratio was approximately 16.49%. Similarly, from 8.04 million to 9.88 million grids, the number of grids increases by approximately 23% and the maximum temperature difference ratio was approximately 5.50%. The temperature difference between the 8.04 and 9.88 million grids was centered in a small area near the middle of the combustion chamber, and the remaining area had temperature difference ratios of less than 5%. In fact, the average temperature difference between the 8.04 and 9.88 million grid numbers was negligible everywhere else, which was sufficient to ensure that the number of grids did not cause significant interference to the simulation results. To ensure computational accuracy and save computational resources, a grid number of approximately 8.04 million was chosen for the subsequent study. Prior to calculation, the model was validated against the test results of the engine by comparing the total pressure loss values simulated by the original combustion chamber with the experimental data. The simulation conditions were chosen to be 20, 40, 60, and 80% of the cruise conditions. As shown on the right side of Figure 7, the simulation results agreed well with the experimental data, with a relative error of less than 4%.

3. RESULTS AND DISCUSSION

3.1. Establishment of Centrifugal Loads. The main goal of studying the HGC was to establish and determine the suitable g-loading value for combustion reactants such that the fuel can be stably burned, the combustion rate can be accelerated, and as uniform an outlet temperature as possible can be provided as well as a uniform temperature prevents turbine damage due to localized overheating. When the swirl inlet is designed, the inlet directs fresh air to the main combustion area. It is necessary to control the g-loading value after the swirl enters the combustion chamber between 500 and 3500 g_0 to avoid flame quenching due to flame instability caused by a g-loading value of more than 3500 g_0,[3,17] while

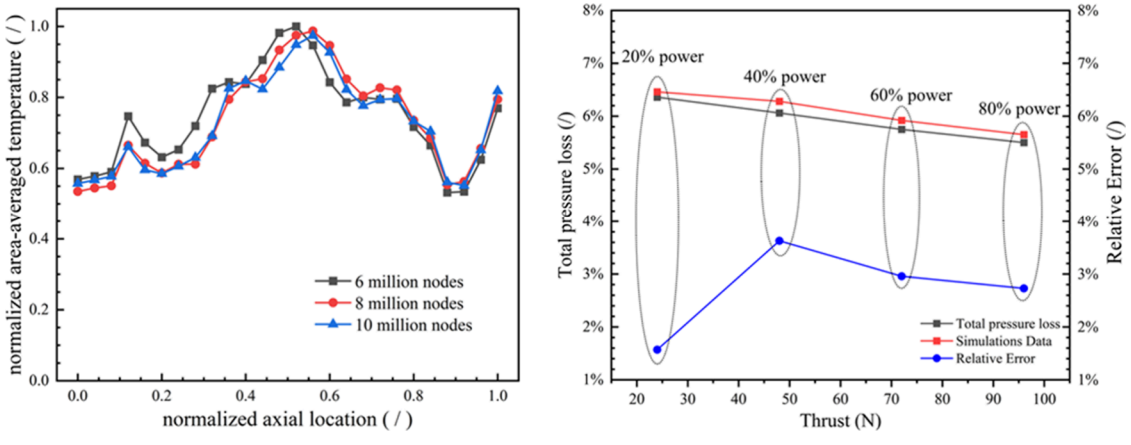

Figure 7. Grid independence (left) and experimental validation (right).

https://doi.org/10.1021/acsomega.4c02030
ACS Omega 2024, 9, 18674−18685

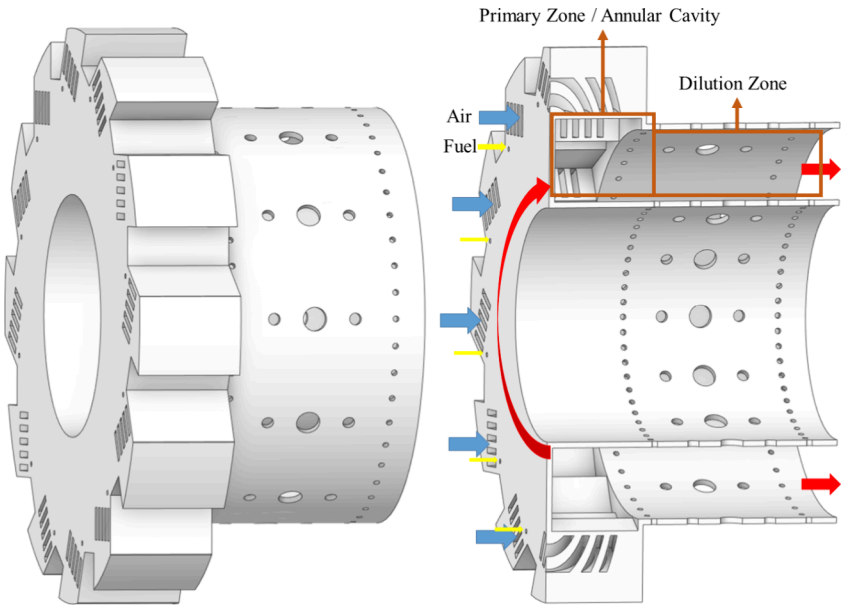

Figure 8. C1 inlet placed horizontally.

simultaneously increasing the *g*-loading value to the maximum possible extent to increase the flame propagation rate. When the inlet area is certain, the higher the inlet flow rate, the higher the inlet velocity and the larger the *g*-loading value.

When the air inlet scheme was designed, it was assumed that the pressurizer was pressurized uniformly around the combustion chamber and had the same pressurization effect on all of the air inlets and air inlet holes. When determining the total mass flow rate of 0.232 kg/s, a total intake area of approximately 4400 mm^2 was used to obtain an injection velocity of 41 m/s. Considering the mean radius of the HGC applied to a micro turbojet engine, a target value of at least 2500 g_0 could be obtained when an inlet tangential velocity of 41 m/s was used. As the angle of inclination increased, the flow and velocity in the combustion chamber decreased and the corresponding *g*-loading value decreased. The average *g*-loading values of the four configurations of the final inlet were in the range of approximately 1840−3600 g_0, in which the inlet flows of C1, C2, and C3 entered the annular cavity with a tangential velocity of approximately 30 m/s. Based on the derivation of eq 1, the *g*-loading value at this time was approximately 1840 g_0, and although the inlet flow velocity of C4 was small, the vortex flow was fully developed, and all four configurations formed a high-*g* environment in the annular cavity that meets the design requirements. However, it is worth noting that there are some locations where the centrifugal load exceeds the recognized flameout limit of 3500 g_0, which can result in partial flameouts.

3.2. Gear-Shaped Air Inlet. In this study, a new HGC structure was designed with an air inlet based on the air inlet holes of the original combustion chamber. A cross-sectional view of C1 is presented in Figure 8. In this configuration, fresh air entered the combustion chamber from the air inlet and the air inlet holes. The air inlet of C1 was placed horizontally on the top wall of the combustion chamber, and most of the air entered the air inlet and was guided to the annular cavity with the outlet being at an angle to shoot the air in a circumferential direction to form a vortex. The rest of the air entered along the axis into the inlet holes in the inner and outer walls to assist in the intake of air. After the main and secondary combustion areas were determined, a baffle was designed between the two areas to increase the residence time of the vortex. This section focuses on the design of the air inlet.

The combustion effects in the four combustion chambers are listed in Figure 9. As shown, the flames of the four

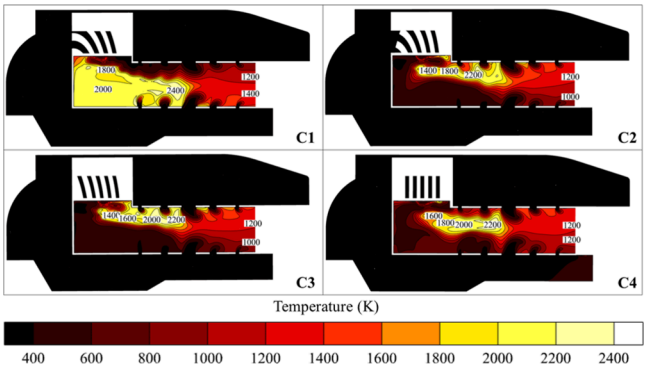

Figure 9. Temperature contours of the four configurations.

combustion chambers were impinged by axial velocities and part of the fuel was transported away from the annular cavity, mixed, and combusted again with the air entering from outside the combustion chamber in the dilution region. Among them, the uniformity of the exit temperature of C4 is shown better. The vortex formed by the inlet of C1 concentrated the flame in the inner corner of the inner wall of the combustion chamber, which is prone to localized overheating, whereas the flames of C2 and C3 were concentrated on the outer wall of the combustion chamber, where the annular cavity connected with the dilution region. The flame position of C4 was between C1, C2, and C3, with the high-temperature combustion region located in the middle of the annular cavity, which prevented the flame from being concentrated on the combustion chamber. In the middle, the flame could not be concentrated on the wall of the combustion chamber and the overall and outlet temperatures showed better uniformity.

3.3. Air Intake Hole Design. The intake holes of C4 were adjusted, keeping the rest of the structure unchanged, and this

https://doi.org/10.1021/acsomega.4c02030
ACS Omega 2024, 9, 18674−18685

new configuration is referred to as C5. The intake ports of C5 remained unchanged and were placed perpendicular to the plane of the combustion chamber. Most of the air entered the intake ports and was guided into the annular cavity, where the outlets were angled to shoot the air out circumferentially to form a vortex. The remaining air entered the inlet holes axially in the inner and outer walls to assist in air intake. Figure 10

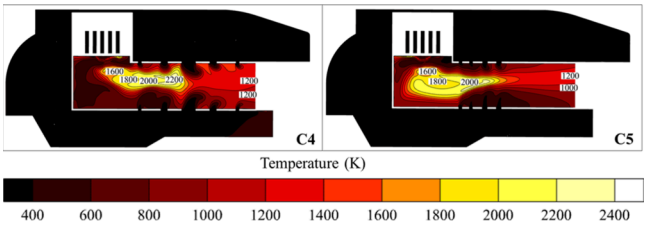

Figure 10. Schematic comparison of the temperature contours for C4 and C5.

shows the combustion of C4 and C5, revealing that the airflow at the air inlet hole had a greater impact on the combustion of the flame in the annular cavity. In the main combustion area from the annular cavity outlet to the middle of the annular cavity, affected by the vortex, the majority of the flame swirled closer to the inner corner of the inner wall of the combustion chamber and the combustion chamber outlet of the flow field distribution was more uniform. The original C4 inlet hole injection of the gas stream formed a larger axial velocity component, part of the gas by the axial velocity component, and the blowing part of the flame downstream, resulting in a nonuniform overall temperature distribution in the combustion chamber. The main dilution area was adjusted toward the annular cavity without changing the total intake area. After redesign of the air intake holes, the overall temperature coefficient of C5 decreased by approximately 65%, which was a remarkable result. All subsequent configurations utilized the adjusted air inlet holes, based on which other configuration options were designed.

3.4. Effect of Baffles on the Flow Field. To further explore the role of the baffle in guiding the flame and improving the uniformity of the exit temperature, the baffle was located between the flow paths, and several modifications were made to C5: As shown in Figure 11, the baffle was located between the annular cavity and the dilution region to maximize the residence time of the high-temperature gas in the annular cavity. The baffle extended from the outer wall to the inner wall of the combustion chamber with lengths of 1 mm (C6), 4 mm (C7), 7 mm (C8), and 10 mm (C9). The four baffle lengths had different effects on the flame. As the baffle length increased, the flame length began to decrease gradually, and although the temperature at the exit plane became more uniform, the baffle caused a reduction in the combustion efficiency.

At a certain flow rate, a baffle that is too long results in a reduced flow area and creates a large backpressure at the inlet, which may result in an inlet stall that can disrupt the mixing of the flame front with the fuel, which led to localized quenching and slowed flame propagation. The overall performance of C7 is better, and the combustion efficiency of C9 performs poorly, although it has a lower pattern factor.

3.5. Overall. In summary, the research and analysis described above led to the finalization of the air inlet hole and baffle research scheme.

Figure 12 shows the combustion of the air inlet hole and the baffle scheme applied to C1−C4. Compared with those in Figure 9, the flames of the four main structural schemes were more fully combusted and the change in the structure of the inlet holes avoided a large amount of fuel blowing into the dilution region The inclusion of the baffle effectively improved the uniformity of the outlet temperature, probably because the baffle could increase the residence time of the swirling flames in the primary zone. The optimization of both structures was beneficial for combustion stability and performance improvement. Figure 13 shows the average circumferential temperatures at the exit planes of the four modified combustion chambers. New-C4 had the best performance in terms of the uniformity of the exit temperature. New-C1 had the high-temperature zone more concentrated at the inner diameter of the annular cavity of the combustion chamber, that is, away from the baffle plate, and the exit plane exhibited a higher temperature at the inner side. The New-C2 and New-C3 high-temperature zones were closer to the top of the outer diameter of the combustion chamber; that is, the high temperatures were concentrated at the baffle plate, where the heat load of the baffle plate is higher. The circumferential position of the exit plane corresponded to a higher outer temperature. There was still a large difference between the average and peak

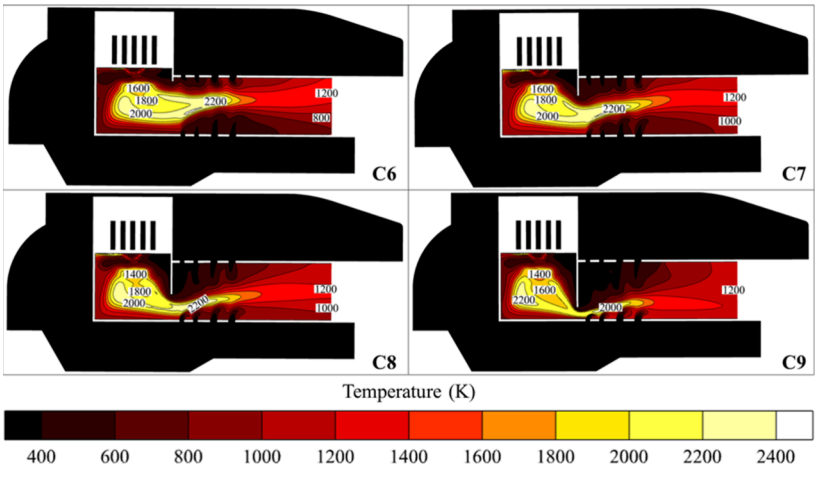

Figure 11. Temperature contours under different baffles.

https://doi.org/10.1021/acsomega.4c02030
ACS Omega 2024, 9, 18674−18685

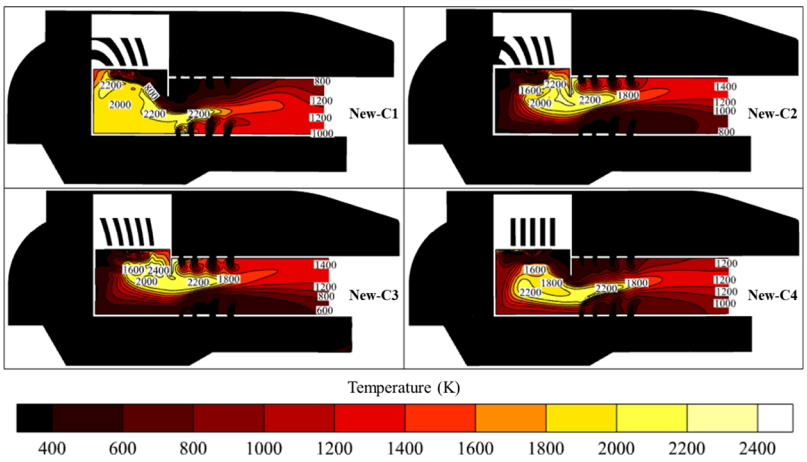

Figure 12. Four new configurations of temperature clouds.

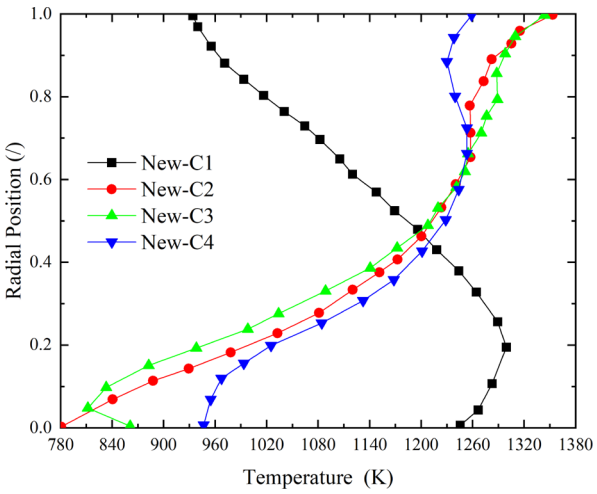

Figure 13. Circumferential mean temperature in the exit plane for the four configurations.

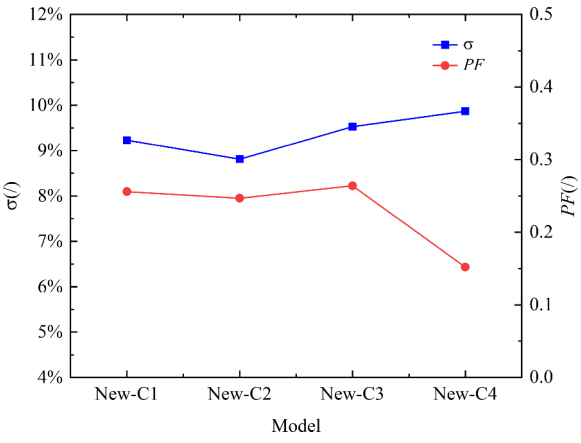

Figure 14. Evaluation parameters for the four configurations.

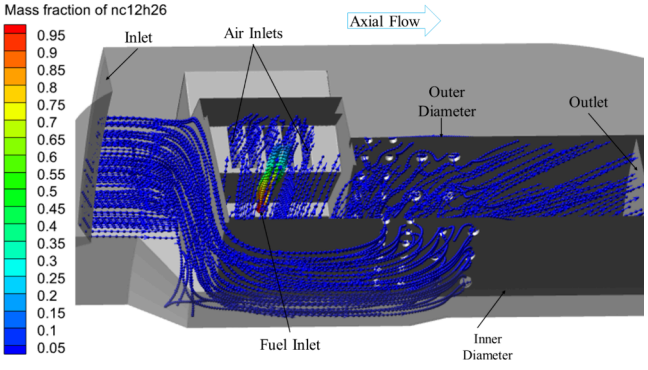

Figure 15. Flow field distribution in New-C4, colored by n-$C_{12}H_{26}$ mass fraction.

temperatures on the outer side, resulting in uneven heating of the turbine, which is prone to localized overheating problems. Moreover, the maximum temperature at the exit of New-C2 and New-C3 is about 1400K, and the thermal load on the bearings is too high, which will also damage the turbine rotor.

The evaluation parameters for the four configurations are compared in Figure 14. The total pressure loss coefficients σ and PF were calculated from the exit-plane results, whereas New-C4 improved the temperature profile in the dilution region of the combustion chamber by increasing the total pressure loss; the Pattern Factor was lower, indicating better overall temperature uniformity. In addition, Figures 12 and 14 show that combustion was accomplished in a relatively short axial distance, with primary combustion in the annular cavity and secondary combustion in the dilution zone; thus, New-C1 and New-C4 will have slightly lower average outlet temperatures than New-C2 and New-C3.

Figure 15 shows the air flow out of the compressor outlet and into New-C4 through the air inlet and intake holes, and the fuel is injected into the annular cavity and positioned at the center. The fuel was rapidly mixed with the air and combusted almost in the circumferential direction, and most of the cyclone was kept in the annular cavity for circumferential movement, and the high temperature gas was discharged in the axial direction after secondary combustion in the dilution zone.

Overall, New-C4 exhibited the best performance. New-C4 was selected as the final solution, and a comparison of the evaluated parameters of New-C4 with those of the original combustion chamber in various aspects is presented in Figure 16. The combustion efficiency of New-C4 has not changed much compared to that of the original combustion chamber, and the uniformity of the outlet temperature has been greatly improved, although the total pressure loss is larger. Moreover, new-C4 obtains smaller axial sizes.

However, the current design remains in the most ideal state for the time being, and there will still be problems in practical application. For example, the evaporator tube in the original

https://doi.org/10.1021/acsomega.4c02030
ACS Omega 2024, 9, 18674−18685

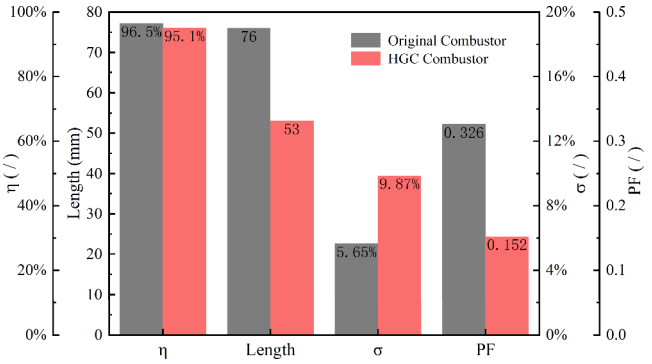

Figure 16. Comparison of the evaluation parameters of the original combustion chamber and New-C4.

combustion chamber is an important component for atomizing liquid fuel and a reasonable atomization method must be found for the HGC. In addition, the mechanism behind the mixing process of the fuel and the air in a high-*g* environment must be further researched.

4. CONCLUSIONS

In this study, a new HGC structure was designed and placed in a 120 N thrust micro turbojet engine and the changes in the overall temperature distribution coefficient and combustion efficiency under different scenarios were compared through simulations. The main conclusions are as follows.

1. The design of the HGC was first centered around the establishment of a highly centrifugal environment in the annular cavity. C1, C2, C3, and C4 retained the intake holes of the original combustion chamber, adopting axial intake ports and intake holes for air intake. The influence of the tilt angle of the air inlet on the establishment of the highly centrifugal environment in the cavity was considered, and the average *g*-loading values of the four schemes for the final air inlet were approximately 1840−3600 g_0.
2. The air intake hole of the original combustion chamber is not suitable for the new structure of the HGC, due to the excessive axial velocity destroying the fuel combustion in the dilution region, stable combustion cannot be achieved, and localized high-temperature regions are also formed at the inlet holes. By designing a new inlet orifice scheme, the airflow can be effectively restricted and the axial velocity component can be reduced by increasing the total pressure loss, which can effectively improve the temperature distribution uniformity in the dilution region. By designing four baffle length schemes to study the vortex residence time and the effect on the flow field, the 4 mm baffle can keep the flow percentage in the annular cavity above 30%, which can effectively increase the residence time of the vortex in the annular cavity.
3. The improved intake orifice and baffle configurations were applied to the four originally designed HGCs. First, the miniature turbojet engines used in the laboratory had 1200K overheat protection and New-C2 and New-C3 had exit temperatures that were too high to be applicable to most of the engines. New-C4 had a higher combustion efficiency than New-C1 and a lower overall temperature distribution coefficient. Compared with the original combustion chamber, New-C4 had better outlet plane temperature uniformity, and better outlet temperature profile performance, although at the expense of total pressure loss.

In addition, adjusting the engine components to match the HGC and without changing the material of the combustion chamber, the axial length of the combustion chamber is saved by at least 30%, the overall engine length is shortened by approximately 11.5%, and the corresponding engine weight is reduced by approximately 10.7%, thereby improving the engine thrust-to-weight ratio by at best 12% at an equal thrust level. Steady-state simulations predicted the feasibility of integrating the HGC into a micro turbojet engine in place of the main combustion chamber and validated the advantages of the HGC as a combustion chamber in terms of shortening the length and improving the temperature uniformity inside the combustion chamber. However, the current design cannot be directly applied to a micro turbojet engine and transient simulations are required to study the flame propagation mechanism in a high-*g* environment and conduct ignition and experimental studies. Overall, the good performance and various advantages of the HGC are worthy of in-depth study, so that it can play an important role in the field of miniature turbojets.

AUTHOR INFORMATION

Corresponding Author

Haozhong Huang − *College of Mechanical Engineering, Guangxi University, Nanning 530004, China;* orcid.org/0000-0001-7181-3840; Email: hhz421@gxu.edu.cn

Authors

Guixin Chen − *College of Mechanical Engineering, Guangxi University, Nanning 530004, China*

Huigui long − *College of Mechanical Engineering, Guangxi University, Nanning 530004, China*

Baijun Lei − *College of Mechanical Engineering, Guangxi University, Nanning 530004, China*

Jianguo Liang − *College of Mechanical Engineering, Guangxi University, Nanning 530004, China*

Complete contact information is available at: https://pubs.acs.org/10.1021/acsomega.4c02030

Notes

The authors declare no competing financial interest.

ACKNOWLEDGMENTS

This work is supported by the National Natural Science Foundation of China (52366007) and the Guangxi Science and Technology Major Project (AA22068103, AA22068104).

NOMENCLATURE

Acronyms

AFRL: Air Force Research Laboratory
FGM: flamelet generated manifold
ITB: inter turbine burner
HGC: high-*g* combustor
RPM: revolutions per minute
TVC: trapped-vortex combustor
UCC: ultra compact combustor

Symbols

C_P: specific heat capacity
d: diameter

https://doi.org/10.1021/acsomega.4c02030
ACS Omega 2024, 9, 18674−18685

g: acceleration
g_0: gravity acceleration
m: mass flow rate
P: pressure
r: radius
S_L: laminar flame speed
T: temperature
η: combustion efficiency
λ: thermal conductivity
u: velocity
ρ: density
τ: time scale
σ: total pressure loss coefficient

REFERENCES

(1) Sirignano, W.; Liu, F. Performance Increases for Gas−Turbine Engines Through Combustion Inside the Turbine. *J. Propul. Power.* **1999**, *15* (1), 111−118.
(2) Lewis, G. D. Centrifugal−Force Effects on Combustion. *Symp. (Int.) Combust.* **1973**, *14* (1), 413−419e.
(3) Zelina, J.; Sturgess, G. J.; Shouse, D. T. The Behavior of an Ultra−Compact Combustor (UCC) Based on Centrifugally−Enhanced Turbulent Burning Rates. In *40th AIAA/ASME/SAE/ASEE Joint Propulsion Conference and Exhibit*, AIAA Fort Lauderdale, FL, 2004; p 3541. DOI: DOI: 10.2514/6.2004-3541.
(4) Hsu, K. − Y.; Goss, L.; Roquemore, W. Characteristics of a Trapped−Vortex Combustor. *J. Propul. Power.* **1998**, *14* (1), 57−65.
(5) Briones, A. M.; Sekar, B.; Shouse, D. T.; Blunck, D. L.; Thornburg, H. J.; Erdmann, T. J. Reacting Flows in Ultra−Compact Combustors With Combined−Diffuser Flameholder. *J. Propul. Power.* **2015**, *31* (1), 238−252.
(6) Zhang, R.; Hao, F.; Fan, W. Combustion and Stability Characteristics of Ultra−Compact Combustor Using Cavity for Gas Turbines. *Applied Energy.* **2018**, *225*, 940−954.
(7) Liu, Y.; Wang, Z.; Tang, H. Numerical Investigation of Turbulent Premixed Combustion in a High Acceleration Field. *J. Therm. Sci. Eng. Appl.* **2020**, *12* (4), No. 041010.
(8) Yonezawa, Y.; Toh, H.; Goto, S.; Obata, M. Development of The Jet−Swirl High Loading Combustor. In *26th Joint Propulsion Conference*, AIAA Orlando,FL,U.S.A, 1990; p 2451. DOI: DOI: 10.2514/6.1990-2451.
(9) Zelina, J.; Shouse, D. T.; Hancock, R. D. Ultra−Compact Combustors for Advanced Gas Turbine Engines. In *Proceedings of the ASME Turbo Expo 2004: Power for Land, Sea, and Air*, ASME Vienna, Austria, 2004; 41669, pp 53−62. DOI: DOI: 10.1115/GT2004-53155.
(10) Zelina, J.; Greenwood, R. T.; Shouse, D. T. Operability and Efficiency Performance of Ultra−Compact, High Gravity (G) Combustor Concepts. In *Proceedings of the ASME Turbo Expo 2006: Power for Land, Sea, and Air*, ASME Barcelona, Spain, 2006; 42363, pp 87−95. DOI: DOI: 10.1115/GT2006-90119.
(11) Sturgess, G.; Zelina, J.; Shouse, D. T.; Roquemore, W. Emissions Reduction Technologies for Military Gas Turbine Engines. *J. Propul. Power.* **2005**, *21* (2), 193−217.
(12) Syred, N.; Claypole, T.; Styles, A. The Role of Centrifugal Force Fields in The Stabilization of Swirling Flames. *J. Energy.* **1982**, *6* (5), 344−345.
(13) Lapsa, A.; Dahm, W. Experimental Study on The Effects of Large Centrifugal Forces on Step−Stabilized Flames. In *5th US Combustion meeting*, Combustion Institute San Diego, CA, 2007, *6* 3388.
(14) Wilson, J. D.; Damele, C. J.; Polanka, M. D. Flame Structure Effects at High G−Loading. *J. Eng. Gas Turbine Power.* **2014**, *136* (10), 101502.
(15) Dwyer, H. A.; Hasegawa, T. Some Flows Associated with Premixed Laminar Flame Propagation in a Rotating Tube Flow. *Proc. Combust. Inst.* **2002**, *29* (2), 1471−1477.
(16) Yan, P.; Fan, W.; Qi, S.; Zhang, R.; Liu, J.; Bai, N.; Zhao, W.; Yang, X. Numerical Investigation on The Effect of G−Load on High−G Ultra−Compact Combustor. *Aerosp. Sci. Technol.* **2022**, *121*, 107305.
(17) Briones, A. M.; Sekar, B.; Erdmann, T. Effect of Centrifugal Force on Turbulent Premixed Flames. *J. Eng. Gas Turbine Power.* **2015**, *137* (1), No. 011501.
(18) Long, B. S.; Briones, A. M.; Stouffer, S. D.; Rankin, B. A. Effect of Rayleigh−Taylor Instability on Backward−Facing−Step Stabilized Turbulent Premixed Flames. In *Proceedings of the ASME Turbo Expo: Power for Land, Sea, and Air*, ASME Charlotte, North Carolina, USA, 2017; Vol. *4B*, p V04BT04A027. DOI: DOI: 10.1115/GT2017-64547.
(19) Greenwood, R. T.; Anthenien, R. A.; Zelina, J. Computational Analysis of The Ultra Compact Combustor. In *43rd AIAA Aerospace Sciences Meeting and Exhibit*, AIAA Reno, NV, 2005; p 220. DOI: DOI: 10.2514/6.2005-220.
(20) Anisko, J. F.; Anthenien, R. A. Jr.; Zelina, J. Numerical Investigation of Cavity−Vane Interactions within The Ultra Compact Combustor. In *44th AIAA Aerospace Sciences Meeting and Exhibit*, AIAA Reno, NV, 2006; p 805. DOI: DOI: 10.2514/6.2006-805.
(21) Conrad, M. M.; Wilson, J. D.; Polanka, M. D. Integration Issues of an Ultra−Compact Combustor to a Jet Turbine Engine. In *49th AIAA/ASME/SAE/ASEE Joint PropulsionConference*, AIAA San Jose, CA, 2013; p 3711. DOI: DOI: 10.2514/6.2013-3711.
(22) Bohan, B. T.; Polanka, M. D. Analysis of Flow Migration in an Ultra−Compact Combustor. *J. Eng. Gas Turbine Power.* **2013**, *135* (5), No. 051502.
(23) Blunck, D.; Shouse, D.; Neuroth, C.; Battelle, R.; Lynch, A.; Sekar, B.; Zelina, J.; Erdmann, T.; Burrus, D.; Howard, R.; Briones, A.; Richardson, D.; Caswell, A. Experimental and Computational Studies of an Ultra−Compact Combustor. In *Proceedings of the ASME Turbo Expo: Power for Land, Sea, and Air*, ASME San Antonio, Texas, USA, 2013; Vol. *1A*, p V01AT04A026. DOI: DOI: 10.1115/GT2013-94372.
(24) Erdmann, T. J. Jr.; Burrus, D. L.; Shouse, D. T.; Gross, J. T.; Neuroth, C.; Caswell, A. W. Experimental Studies of a High−G Ultra−Compact Combustor at Elevated Pressures and Temperatures. In *54th AIAA Aerospace Sciences Meeting*, AIAA San Diego, California, USA, 2016; p 0446.
(25) Cottle, A. E.; Polanka, M. D.; Goss, L. P.; Goss, C. Z. Investigation of Air Injection and Cavity Size Within a Circumferential Combustor to Increase G−Load and Residence Time. *J. Eng. Gas Turbine Power.* **2018**, *140* (1), No. 011501.
(26) Bohan, B. T.; Polanka, M. D.; Rutledge, J. L. Computational Analysis of a Novel Cooling Scheme for Ultra Compact Combustor Turbine Vanes. In *Proceedings of the ASME Turbo Expo: Power for Land, Sea, and Air*, ASME Charlotte, North Carolina, USA, 2017; Vol. *5C*, p V05CT17A002. DOI: DOI: 10.1115/GT2017-63319.
(27) DeMarco, K. J.; Bohan, B. T.; Polanka, M. D.; Rutledge, J. L.; Akbari, P. Analysis of an Additively Manufactured Cooled Ultra Compact Combustor Vane. *J. Therm. Sci. Eng. Appl.* **2019**, *11* (5), No. 051021.
(28) Bohan, B. T.; Polanka, M. D. A New Spin on Small−Scale Combustor Geometry. *J. Eng. Gas Turbine Power.* **2019**, *141* (1), No. 011504.
(29) Bohan, B. T.; Polanka, M. D. Experimental Analysis of an Ultra Compact Combustor Powered Turbine Engine. In *Proceedings of the ASME Turbo Expo: Power for Land, Sea, and Air*, ASME Phoenix, Arizona, USA, 2019; Vol. *4A*, p V04AT04A037. DOI: DOI: 10.1115/GT2019-90607.
(30) Liu, Y.; Wang, Z.; Tang, H. A New Design of a Pinwheel−Shaped High−G Combustor. *J. Eng. Gas Turbine Power.* **2021**, *143* (9), No. 091020.
(31) Pioro, I. L., Duffey, R. B. Appendix D: Sample of Uncertainty Ana−lysis. In *Heat Transfer and Hydraulic Resistance at Supercritical Pressures in Power Engineering Applications*; ASME Press, New York, 2007; pp 247−267.

https://doi.org/10.1021/acsomega.4c02030
ACS Omega 2024, 9, 18674−18685

(32) Sirjean, B.; Dames, E.; Sheen, D. A.; You, X.-Q.; Sung, C.; Holley, A. T.; Egolfopoulos, F. N.; Wang, H.; Vasu, S. S.; Davidson, D. F.; Hanson, R. K.; Pitsch, H.; Bowman, C. T.; Kelley, A.; Law, C. K.; Tsang, W.; Cernansky, N. P.; Miller, D. L.; Violi, A.; Lindstedt, R. P., *A High−Temperature Chemical Kinetic Model of N−Alkane Oxidation*, JetSurF Ver. 1.0, 2009, http://web.stanford.edu/group/haiwanglab/JetSurF/JetSurF1.0/index.html.

(33) Cottle, A. E.; Polanka, M. D. Numerical and Experimental Results From a Common−Source High−G Ultra−Compact Combustor. In *Proceedings of the ASME Turbo Expo: Power for Land, Sea, and Air*, Seoul, South Korea, ASME 2016; Vol. *4A*, p V04AT04A013.

(34) SAE E-31 Technical Committee *Procedure for the analysis and evaluation of gaseous emissions from aircraft engines*. SAE ARP1533B **2013**.

(35) Mattingly, J. D. Elements of Propulsion: Gas Turbojets and Rockets. *AIAA* **2006**, 765−766.

(36) Celik, I. B.; Ghia, U.; Roache, P. J.; Freitas, C. J. Procedure for Estimation And Reporting of Uncertainty Due to Discretization in CFD Applications. *J. Fluids Eng.-Trans. ASME* **2008**, *130* (7), No. 078001, DOI: 10.1115/1.2960953.

https://doi.org/10.1021/acsomega.4c02030
ACS Omega 2024, 9, 18674−18685